scientific reports

OPEN

Photocatalytic water splitting and charge carrier dynamics of Janus PtSSe/ζ-phosphorene heterostructure

Poonam Chauhan & Ashok Kumar[✉]

On the basis of first-principles calculations and non-adiabatic molecular dynamics (NAMD) simulations, we explore the photocatalytic water splitting properties of PtSSe/ζ-Phosphorene heterostructure. This heterostructure possess semiconducting nature with high carrier mobility ($\approx 10^3$ cm^{2}V^{-1}s^{-1}). The calculated high value of electron-hole recombination rate as compared to electron transfer rate and hole transfer rate, establish the Type-II mechanism more favorable for PtSSe/ζ-Phosphorene heterostructure. Further, the calculated value of solar-to-hydrogen (STH) conversion efficiency of PtSSe/ζ-Phosphorene exceeds to 10%, which makes it the potential candidate for commercial production of hydrogen for industrial use. STH conversion efficiency is further tunable on rotating one monolayer over other with specific angles in the heterostructure. Our study demonstrates PtSSe/ζ-Phosphorene heterostructure to be efficient Type II-scheme photocatalyst for water splitting.

The photocatalysts materials gathered researcher's attention due to their stupendous ability to breakdown water by utilizing solar energy and produce hydrogen with pollution-free zero by-products[1]. Due to superior physical and chemical properties of two-dimensional (2D) monolayer materials, they act as potential candidates for photocatalytic water splitting[2–4]. The high carrier's recombination rate and narrow optical absorption, limits the use of 2D materials as photocatalyst for water splitting[5], however, the 2D van der Waals heterostructures (vdWHs) can overcome the limitation of 2D monolayers for water splitting[6–8].

To evaluate the staggered arrangement of valance band maximum (VBM) and conduction band minimum (CBM) of each monolayers in conjunction with the built-in electric field (EF) in vdWHs, the two photocatalytic mechanisms namely Type-II[9] and Z-scheme[10] are implemented in the heterostructures. The accumulation of electrons and holes on different monolayer surface of heterostructures results in reduction and oxidation reaction of water splitting for both Type-II and Z-scheme, however, the charge transfer pathways remains different for these mechanisms[9]. Both the mechanisms possess excellent carrier utilization capability; however, Type-II is limited by low redox ability. Thus Z-scheme is preferred over Type-II for the high redox ability and high solar-to-hydrogen (STH) conversion efficiency[11].

The presence of EF in the heterostructure and non-adiabatic coupling (NAC) of photogenerated charge carriers are the key parameters that influence the STH conversion efficiency of heterostructure photocatalysts[12]. The presence of EF in the heterostructure provide additional degree of freedom to tailor the photocatalytic properties of photocatalyst materials[13,14]. Stronger the NAC between the interface photogenerated charge carriers, more rapidly the charge carriers combine that results into a decrease in the STH conversion efficiency. The NAC effect in vdWHs is demonstrated in previous studies[15–19]. Also, the different stacking patterns significantly affects the NAC between the charge carriers[20,21].

The experimental synthesis 2D Janus PtSSe monolayer[22] and tendency of occurring phosphorene in a variety of allotropic forms[23–25] motivated to investigate the Janus PtSSe/ζ-Phosphorene heterostructure. Due to difference in the electronegativity of surface atoms in Janus PtSSe, an intrinsic electric field get induced which is beneficial to improve photocatalytic water splitting properties[26]. Besides Janus PtSSe monolayer, the α- and β-phosphorene synthesized experimentally[23,24] and the various stable allotropes such as γ, δ, ζ, red, hexa and ψ-phosphorene are predicted using density functional theory[25].

However, the phosphorene is thermodynamically less stable as comparison to its oxide (P$_2$O$_5$) or phosphates. The stability of these compounds can be attributed to the strong P$=$O bonds in P$_2$O$_5$ and the robust P-O bonds in phosphates[27]. Also, the weak van der Waals forces between phosphorene layers make it prone to structural

Department of Physics, Central University of Punjab, VPO Ghudda, Bathinda 151401, India. [✉]email: ashokphy@cup.edu.in

instability[28]. The phosphorene stability is also affected by environmental conditions such as moisture and oxygen that accelerates its degradation[28]. Despite of that the stability of phosphorene is enhanced by various methods such as chemical functionalization, doping with metals, and creating 2D heterostructures[29]. These modifications can enhance both the stability and catalytic activity of phosphorene for water splitting[29]. Under different ambient condition, various oxide configuration of phosphorene are stable[27]. Also, the van der Waals substrate and vertical electric field significantly enhance the stability of phosphorene by suppressing oxidation[30].

Despite of that, the ζ- phase of phosphorene which is dynamically and thermally stable[31], has not been much explored. Herein, various stacking patterns of the heterostructure of Janus PtSSe with ζ-phosphorene are considered, out of which energetically most stable configuration of heterostructure is adopted for further study. The thermal stability of the heterostructure is confirmed using ab initio molecular dynamics (AIMD) simulations. Non-adiabatic molecular dynamics (NAMD) simulations[32], are adopted to estimate the electron transfer, hole transfer and recombination rate of photogenerated charge carriers. Gibbs free energy profiles are obtained to evaluate hydrogen evolution reaction (HER) and oxygen evolution reaction (OER) on the surface of vdWHs. Also, the experimental and theoretical feasibility of rotation of one monolayer over other monolayer at large angles[33–35], we inspect the effect of specific rotation on the electronic properties and STH conversion efficiency of PtSSe/ ζ-phosphorene heterostructures is also demonstrated.

Computational details

All the simulations of PtSSe/ζ-Phosphorene heterostructure are performed using *Vienna ab initio simulation package* (VASP)[36,37]. To include electrons and ions interactions, we used projected augmented-wave (PAW) potentials, while generalized gradient approximation (GGA) parameterized by Perdew-Burke-Ernzerhof (PBE) has been implemented to calculate exchange-correlation functionals[38]. The electronic band structure and bands alignments are also obtained using HSE06 hybrid functional. The structures were relaxed until the Hellmann-Feynman forces decrease below 0.01 eV/Å. The energy convergence criteria between sequential steps for structural relaxation was fixed at 10^{-5} eV. For the sampling of the Brillouin zone, the Γ-centred k-mesh of $12 \times 12 \times 1$ has been implemented[39]. A vacuum of ~ 25 Å is used to exterminate the interactions between neighbouring images along perpendicular direction. To model the vdW interactions between the monolayers in heterostructures, DFT-D3 method[40] was implemented in the calculations. AIMD simulations controlled by Nose-Hoover thermostat[41,42] under NVT ensemble were performed using $3 \times 3 \times 1$ supercell up to 5 ps with time step of 3 fs. For the optical absorption spectra, $32 \times 32 \times 1$ k-point grid was used in the calculations. NAMD simulations were performed within decoherence-induced surface hopping (DISH) method as implemented in Hefei-NAMD package[43]. We sampled 4000 trajectories for the simulation in DISH method. We also included the solvent effect in Gibbs free energy calculations. The rotation of one layer over other in heterostructure is demonstrated using the method proposed by Lazic et al.[44]. The number of atoms in the calculations corresponding to 4^0, 8^0 and 12^0 rotation are 220, 170 and 186, respectively. The information about the calculations of excitonic binding energy, Gibbs free energy and STH conversion efficiency is provided in ESI.

Results and discussion

The Janus PtSSe monolayer possess trigonal structure with hexagonal unit cell, while ζ-phosphorene possess the rectangular unit cell. Their lattice parameters (a = b = 3.66 Å for PtSSe; and a = 6.40 Å and b = 5.25 Å for ζ-Phosphorene) are consistent with the literature[45–47]. The AIMD simulations confirm their thermodynamic stability as depicted in Fig. S1. Both PtSSe and ζ-Phosphorene monolayers are indirect bandgap semiconductor having bandgap value of 1.52 eV and 1.20 eV, respectively (Fig. S2), which are also consistent with literature[47,48]. Furthermore, the average electrostatic potential curves of these monolayers are depicted in Fig. S3.

Next, a Janus PtSSe/ζ-Phosphorene heterostructure is generated in rectangular unit cell (Fig. 1 (a) and Fig. S4 (a)) having 34 atoms with minimal lattice mismatch (along a = 1.84% and along b = 4.23%). The lattice
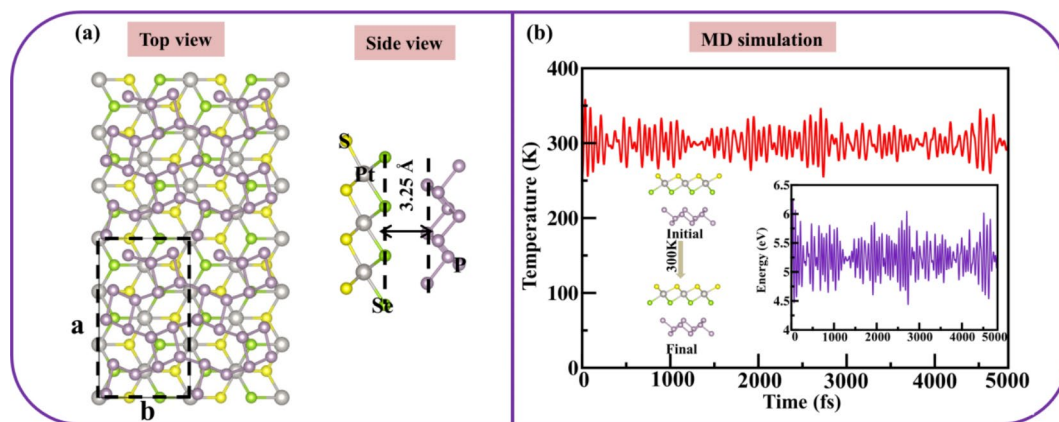

Fig. 1. **(a)** Structure (top view and side view) and **(b)** *AIMD* simulation curves representing the fluctuation of energy with time step along with initial and final structure corresponding to Se-side contacting ζ-Phosphorene of PtSSe/ζ-Phosphorene heterostructure.

parameter of heterostructure unit cell is: a = 6.59 Å and b = 11.41 Å. Seven different types of stacking patterns of PtSSe/ζ-Phosphorene heterostructure are considered, out of which AA stacking is more stable as depicted in Fig. S5. Therefore, AA-stacked heterostructure is considered for further study. The interlayer distance of most stable stacked heterostructure is calculated to be 2.96 Å and 3.25 Å corresponding to S-side and Se-side of PtSSe contacting ζ-Phosphorene. To determine the energetically stability of PtSSe/ζ-Phosphorene heterostructure, the binding energy is calculated as: $E_b = E_{PtSSe/ζ-Phosphorene} - (E_{PtSSe} + E_{ζ-Phosphorene})$; where $E_{PtSSe/ζ-Phosphorene}$, E_{PtSSe} and $E_{ζ-Phosphorene}$ are the total energy of PtSSe/ζ-Phosphorene heterostructure, PtSSe monolayer and ζ-Phosphorene monolayer, respectively. The binding energy of PtSSe/ζ-Phosphorene heterostructure is calculated to be -23.82 meV/Å² and − 22.66 meV/ Å² corresponding to S-side and Se-side contacting ζ-Phosphorene, which is comparable with most common vdW crystals graphite (-12 meV/Å²)[49] and MoS$_2$ (-26 meV/Å²)[50], which indicates that PtSSe/ζ-Phosphorene heterostructure is dominated by the vdW interactions. The electrostatic potential difference between two surfaces of PtSSe/ζ-Phosphorene heterostructures is obtained to be 0.5 eV and a charge of 0.028 electron/atom is accumulated around the Se atom of PtSSe (Fig. S6).

Furthermore, the mechanical stability of vdWH is quantified by computing Young's modulus (Y_{2D}), Poisson ratio (ν), and elastic constants (C_{ii}). PtSSe/ζ-Phosphorene heterostructure satisfies the Born and Huang requirements (C_{11} (= 94.71 N/m) > $|C_{12}|$ (= 25.03 N/m) and $C_{66} = (C_{11} - C_{12})/2 > 0$)[51], confirming its mechanical stability. The calculated value of Youngs modulus of PtSSe/ζ-Phosphorene heterostructure is 88.07 N/m. The Poisson ratio (ν = 0.25) indicates PtSSe/ζ-Phosphorene heterostructure to be brittle in nature according to Frantsevich rule (ν < 1 /3)[52]. Next, the thermal stability of vdWH is determined by AIMD simulations as depicted in Fig. 1 (b) and Fig. S4 (b). The fluctuation of temperature and energy is around a constant value of temperature and energy w.r.t. the time steps. The initial and final structure of heterostructure is maintained without any distortion along with nearly the same interlayer distance of vdWH.

Next, the electronic structure is obtained at HSE06 level of theory and the calculated value of bandgap is 0.67 eV and 0.80 eV corresponding to S-side and Se-side contacting ζ-Phosphorene as shown in Fig. S7. Now, we implement Z-scheme and Type-II mechanism[53] to investigate the band alignment of PtSSe/ζ-Phosphorene heterostructure for photocatalytic water splitting. In Z-scheme mechanism, the recombination of photogenerated charge carriers takes place at upper VBM and lower CBM in vdWH as depicted in Fig. 2 and Fig. S8 corresponding to Se-side and S-side, respectively. The VBM of ζ-Phosphorene and CBM of PtSSe properly engulf the redox potential of water and recombination of charge carriers takes place in between the VBM of PtSSe and CBM of ζ-Phosphorene. While in Type-II mechanism, the electron transfer takes place in between higher CBM to lower CBM and transfer of holes takes place in between lower VBM to higher VBM (Fig. 2 and Fig. S8).

In order to evaluate the different charge transfer pathways, interlayer transfer of electrons and holes are investigated by utilizing NAMD simulations and evaluating the time-dependent Kohn-Sham (TDKS) equation at different time T corresponding to Kohn-Sham (KS) orbitals, $\psi_E(r, T)$, as[43]:
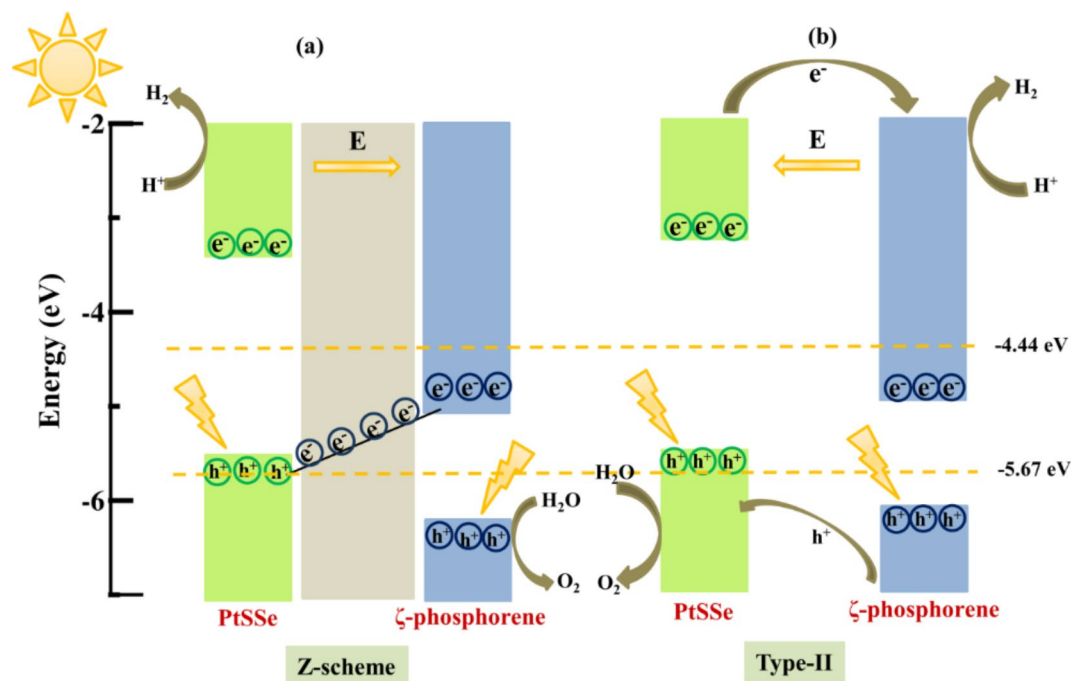

Fig. 2. Band alignments of PtSSe/ζ-Phosphorene heterostructure within (a) Z-scheme and (b) traditional Type-II mechanism at HSE06 level of theory corresponding to Se-side of PtSSe contacting ζ-Phosphorene. The VBM and CBM of PtSSe and ζ-Phosphorene monolayers are shifted by vacuum potential. The orange dashed lines correspond to water redox potential and E is built-in electric field in heterostructure.

$$\psi_E(r, T) = \sum_k C_k(T)\, \phi_k(r, R(T)) \tag{1}$$

The electron transfer, hole transfer and electron-hole recombination at VBM, CBM and VBM-CBM interface is represented by 1, 2 and 3 in KS orbital plot (Fig. 3). The photogenerated charge carriers recombination rate depends upon decoherence time (D_T) and NAC[43]. The calculated value of decoherence time is 19.67 fs. Lesser the decoherence time, higher is the carrier's recombination rate. Further, the NAC of charge carriers is evaluated as:

$$d_{xy} = \left\langle \psi_x \left| \frac{\partial}{\partial t} \right| \psi_y \right\rangle = \frac{\langle \psi_x | \nabla_r H | \psi_y \rangle}{\varepsilon_y - \varepsilon_x} \dot{r} \tag{2}$$

where $\dot{r}$ is the velocity of the nuclei. NACs is calculated by electron-phonon coupling elements ($\langle \psi_x | \nabla_r H | \psi_y \rangle$), the energy gap ($\varepsilon_y - \varepsilon_x$) and velocity ($\dot{r}$). The calculated value of NAC for electron-hole recombination (7.38 meV) is higher than the electron transfer (5.35 meV) and hole transfer (2.02 meV), that may lead to the high electron-hole recombination rate. The similar trend of NAC is also appeared in CrS_3/GeSe[15] and Sc_2Cl_2/Hf_2CO_2[10] heterostructures.

Next, we calculate the electron transfer rate, hole transfer rate and electron-hole recombination rate by employing DISH algorithm to include the effect of quantum coherence in the calculations[54,55]. The electron-hole recombination rate (τ) for the full exponential decay process is formulated as[56]:

$$P(T) = \exp\left(\frac{-T}{\tau}\right) \tag{3}$$

The calculated value of electron transfer and holes transfer rate is 12.23 ps (Fig. 4 (a)) and 32.21 ps (Fig. 4 (b)), respectively. The recombination of VBM of PtSSe and CBM of ζ-phosphorene takes place in 48.16 ps as depicted in Fig. 4 (c), which is higher than CrS3/GeSe (6.24 ps) and[15] copper-nickle sulphide/ g-C_3N_4 (36.9 ps) heterostructures[57]. The results of NAMD simulations suggest that electron transfer and holes transfer are much faster than electron-hole recombination, which suggests that PtSSe/ζ-phosphorene heterostructure follows traditional Type-II mechanism for water splitting[12,58,59].

Next, the charge carrier mobility is calculated to explore the migration capability of charge carriers using deformation potential theory[60,61]:
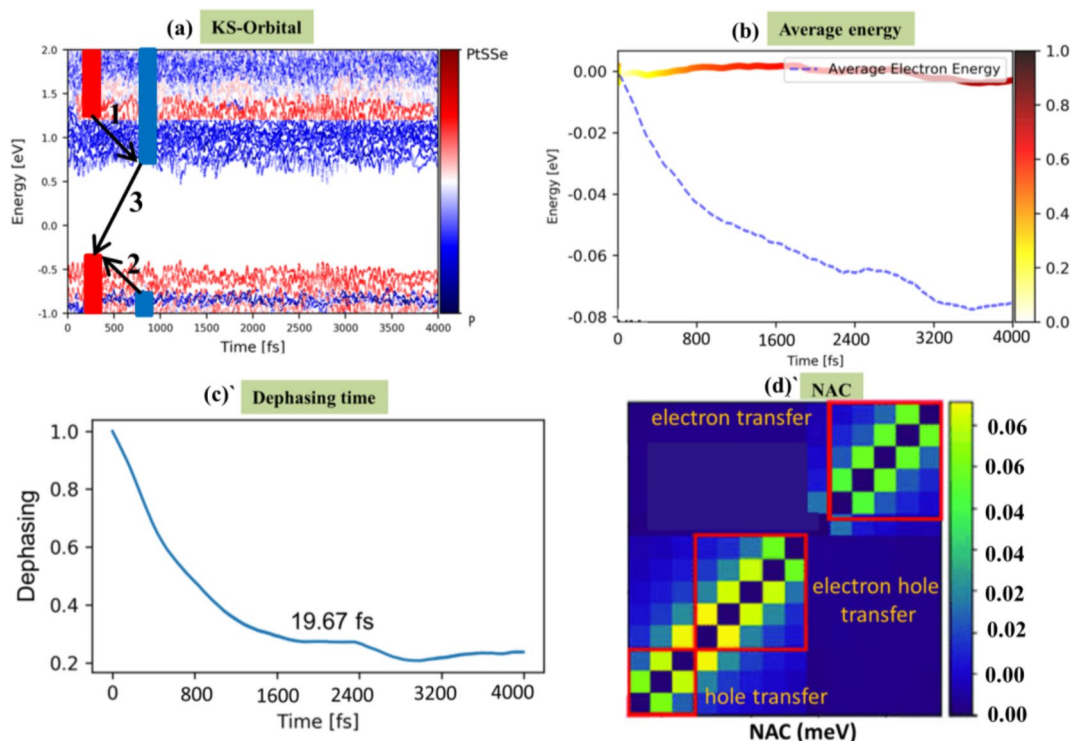

Fig. 3. **(a)** Kohn-sham energy orbitals, **(b)** average energy, **(c)** dephasing time and **(d)** non-adiabatic coupling (NAC) corresponding to Se-side contacting ζ-Phosphorene of PtSSe/ζ-Phosphorene heterostructure. In KS-Orbital energy plots, the blue and red energy levels correspond to the PtSSe and ζ-Phosphorene, respectively. 1, 2 and 3 in Kohn-Sham energy levels represent the electron transfer, hole transfer and electron-hole recombination.
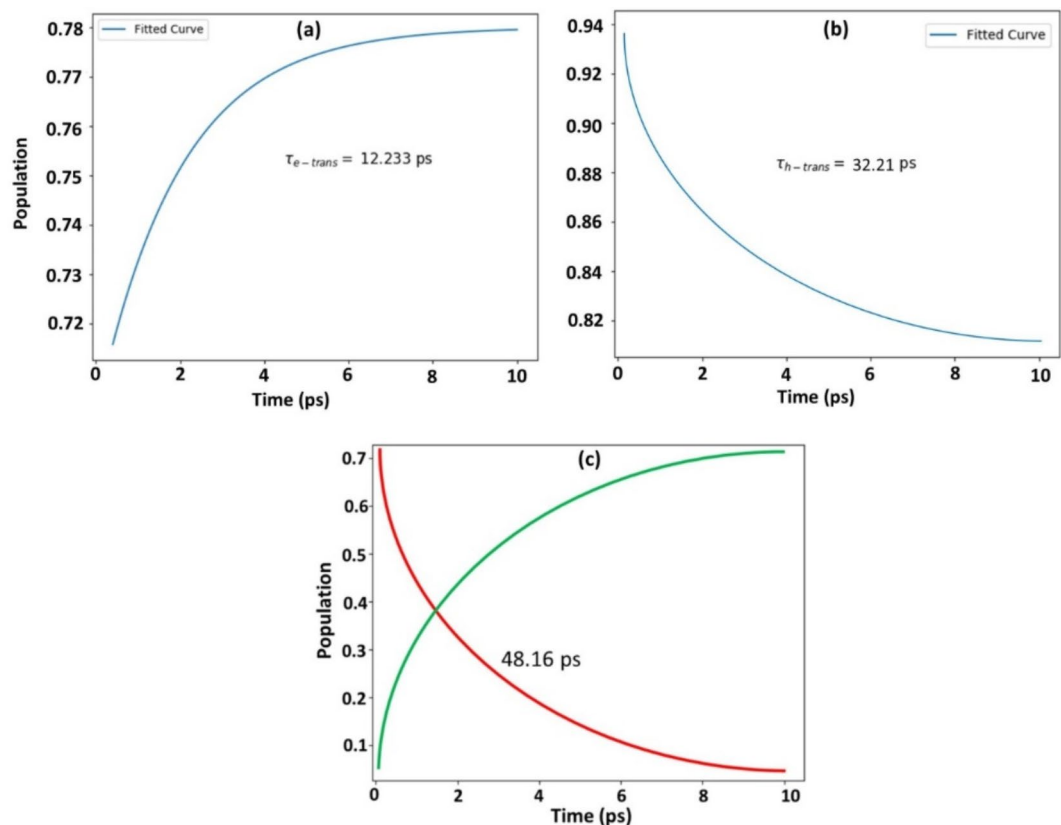
Fig. 4. (a) Electron transfer rate, (b) hole transfer rate and (c) recombination rate corresponding to Se-side of Janus PtSSe contacting ζ-Phosphorene in PtSSe/ζ-Phosphorene heterostructure.

$$\mu_c = \frac{e\hbar^3 C^{2D}}{K_B T m m^* E_d^2} \tag{4}$$

where μ_c represents the carrier mobility, m is the effective mass, C^{2D} is the elastic modulus and E_d is the deformation potential. The calculated value of electrons mobility comes out to be 10^3 cm^{2}V^{-1}s^{-1}. Note that the carrier mobility of ζ-Phosphorene and Janus PtSSe monolayers is calculated to be 10^2 cm^{2}V^{-1}s^{-1} (Table S1). The details of carrier mobility calculations are given in ESI (Fig. S9 and Table S1).

Further to investigate the light harvesting ability of PtSSe/ζ-Phosphorene, the optical absorbance spectra is calculated from the imaginary part of the dielectric function as[62,63]:

$$A(\omega) = \frac{\omega}{c} L \varepsilon_{imaginery}(\omega) \tag{5}$$

Where, L is the length of unit cell in Z-direction. From the computed optical absorption spectra of heterostructure and monolayers, it is observed that the first most prominent peak lies in the visible region (Fig. S10). Also, the PtSSe/ζ-Phosphorene heterostructure possess low value of excitonic binding energy as compare to monolayers of Janus PtSSe and ζ-Phosphorene, which is favorable factor for spatial separation of charge carriers. The detailed calculation of excitonic binding energy is provided in ESI.

Next, the stability of PtSSe/ζ-Phosphorene heterostructure photocatalyst in aqueous solution is accessed by calculating thermodynamic oxidation (Φ^{ox}) and reduction potential (Φ^{re}) using the method proposed by Chen and Wang[64]. The calculated value of reduction (oxidation) potential -1.29 eV (3.61 eV) is higher (lower) than the reduction potential of H$^+$/H$_2$ (oxidation potential O$_2$/H$_2$O), that indicates the stability of PtSSe/ζ-Phosphorene heterostructure in the aqueous solution. The detailed discussion of calculation of oxidation and reduction potential is provided in ESI.

Furthermore, the feasibility of adsorption of water molecule on the heterostructure surfaces is accessed by calculating water adsorption energy as: $E_{adsorption} = E_{*H_2O} - E_* - E_{H_2O}$. The calculated value of adsorption energy is $\approx$ -0.5 eV. The negative value adsorption energy indicates the feasibility of adsorption of water molecules on the surfaces of PtSSe/ζ-Phosphorene heterostructure. The atomic adsorption models of water molecule on different surfaces of heterostructure are shown in Fig. S11.

Next, to access the feasibility of the oxidation and reduction half reactions for water splitting on PtSSe/ζ-Phosphorene heterostructure surfaces, the Gibbs free energy profile are obtained using the method proposed by Nørskov et al.[65] The details of the calculations of Gibbs free energy is provided in ESI (Table S2). The potential
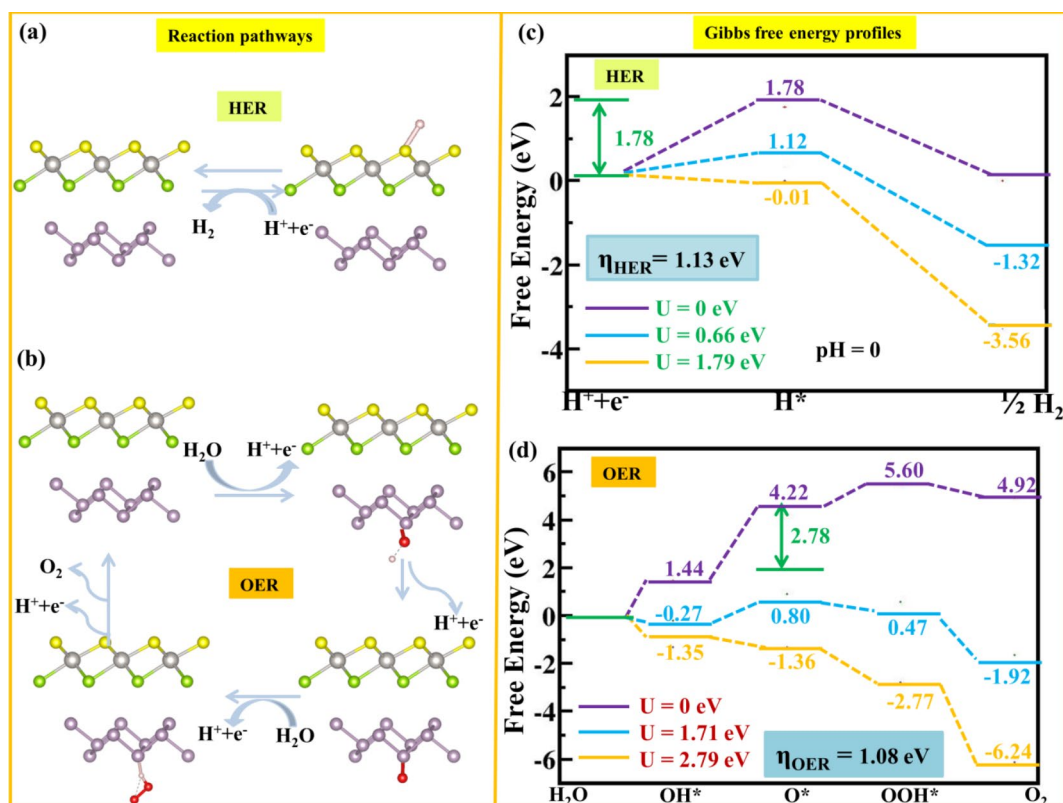
Fig. 5. The reaction pathways and Gibbs free energy profiles of HER and OER for the Z-scheme corresponding to Se-side contacting ζ-Phosphorene in PtSSe/ζ-Phosphorene heterostructure. Color code: white sphere = H-atom; red sphere = O-atom, Green sphere = Se-atom, Yellow sphere = S-atom and silver sphere = Pt atom and dark grey sphere = P-atom, respectively). The violet and sky blue lines specify the circumstances in the absence and presence of light irradiation (at the potential of photogenerated carriers), respectively, while the orange lines represent the situation with required external potentials.
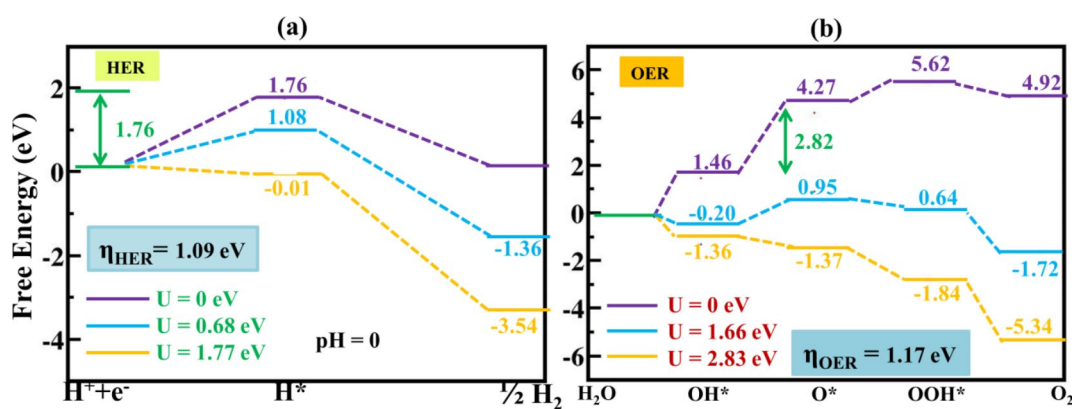

Fig. 6. Gibbs free energy profiles of (a) HER and (b) OER for Se-side contacting PtSSe/ζ-Phosphorene heterostructure in Type-II scheme. Color code: white sphere = H-atom; red sphere = O-atom, Green sphere = Se-atom, Yellow sphere = S-atom and silver sphere = Pt atom and dark grey sphere = P-atom, respectively). The violet and sky blue lines specify the circumstances in the absence and presence of light irradiation (at the potential of photogenerated carriers), respectively, while the orange lines represent the situation with required external potentials.

for the photogenerated electrons (holes) was obtained by the difference between the potential of CBM (VBM) and the reduction potential of water at HSE06 level of theory. The computed values of photogenerated electron potential and holes potential corresponding to Se-side contacting ζ-Phosphorene in heterostructure for Type-II scheme (Z-scheme) are 0.68 eV (0.66 eV) and 1.66 eV (1.71 eV), respectively (Figs. 5 and 6). On the other

hand, the computed values of photogenerated electron potential and holes potential corresponding to S-side contacting ζ-Phosphorene in heterostructure for Type-II scheme (Z-scheme) are 0.67 eV (0.64 eV) and 1.65 eV (1.69 eV), respectively (Fig. S12).

For the spontaneous process of HER to occur on the Se-side of PtSSe contacting ζ-Phosphorene in heterostructure surface required an extra potential of 1.09 eV and 1.13 eV for Type-II and Z-scheme mechanism, respectively. Further, for spontaneous OER processes, an extra potential of 1.17 eV and 1.08 eV is required in Type-II and Z-scheme mechanism (Figs. 5 and 6), respectively. The required extra OER potential for PtSSe/ζ-Phosphorene is lower than β-PtSSe (1.27 eV)[66], GaAs (1.39 eV)[67] and g-C_3N_4 (1.45 eV)[68].

Next, the STH conversion efficiency of PtSSe/ζ-Phosphorene heterostructure photocatalyst for type-II mechanism is calculated as:[69]

$$\eta'_{STH} = \frac{\Delta G \int_E^\infty \frac{E(\hbar\omega)}{\hbar\omega} d(\hbar\omega)}{\int_0^\infty E(\hbar\omega) d(\hbar\omega) + \Delta V \int_{E_g}^\infty \frac{E(\hbar\omega)}{\hbar\omega} d(\hbar\omega)} \quad (6)$$

The STH conversion efficiency of PtSSe/ζ-Phosphorene heterostructure photocatalyst for Z-scheme is calculated as:[70]

$$\eta'_{STH} = \frac{1}{2} \frac{\Delta G \int_E^\infty \frac{E(\hbar\omega)}{\hbar\omega} d(\hbar\omega)}{\int_0^\infty E(\hbar\omega) d(\hbar\omega) + \Delta V \int_{E_g}^\infty \frac{E(\hbar\omega)}{\hbar\omega} d(\hbar\omega)} \quad (7)$$

Where, E_g is the larger of the bandgap of monolayer projected in heterostructure and E is the energy of photon utilized to proceed water splitting mechanism feasible. The details of the STH calculations are given in ESI. The calculated value of STH conversion efficiency for Se-side and S-side contacting ζ-Phosphorene in PtSSe/ζ-Phosphorene heterostructure for Type- II mechanism is 24.86% and 23.96%, respectively, whereas for the Z-scheme mechanism it is calculated to be 12.43% and 11.98%, respectively.

Next, we study the role of rotation of one monolayer over other in heterostructure, on the electronic band structure and band alignments. The one monolayer over other in the heterostructure is rotated at 4^0, 8^0 and 12^0. The top view and side view of heterostructure at different rotation is shown in Fig. S13. Further the thermodynamic stability of these heterostructures are demonstrated in the terms of AIMD simulations in NVT ensemble. The smaller fluctuation of temperature around a constant level with respect to time steps confirms their thermal stability as depicted in Fig. S14. The atomic configuration of these monolayers remains undistorted after heating systems at 300 K.

The electrostatic potential energy difference of PtSSe and ζ-Phosphorene decreases as the different angle of rotation as depicted in Fig. S15 and the 0.028 electron/atom, 0.035 electron/atom and 0.31 electron/atom charge accumulated around Se atom, respectively at 4^0, 8^0 and 12^0 rotations. The electronic band structure at different rotation angle is shown in Fig. S16 and Table S3. Due to change in the bandgap value, the corresponding change in the VBM and CBM of Janus PtSSe, ζ-Phosphorene and PtSSe/ζ-Phosphorene heterostructure is observed. PtSSe/ζ-Phosphorene heterostructure at different angle of rotation shows proper band alignment for water splitting as depicted in Fig. S17. The photogenerated potential for electron (U_e) and holes (U_h) at different angle of rotations illustrated in Table S4. The photogenerated potential of holes are higher than electron potential. The conduction band offsets of PtSSe and ζ-Phosphorene modifies on rotation, that results into change in the STH conversion efficiency of heterostructure.

Conclusions

In summary, we designed the thermally stable PtSSe/ζ-Phosphorene heterostructure for efficient photocatalytic water splitting. PtSSe/ζ-Phosphorene possess suitable band alignment for water splitting with high carrier mobility ($\approx 10^3$ cm^{2}V^{-1}s^{-1}). Moreover, the most prominent peak of optical absorption spectra lies in visible region. The calculated value of recombination, electron transfer and holes transfer rate of photogenerated charge carrier is 48.16 ps, 12.23 ps and 32.21 ps, respectively. The higher value of electron-hole transfer rate as compared to the electron-transfer and hole-transfer suggested Type-II scheme mechanism more suitable for PtSSe/ζ-Phosphorene heterostructure. The STH conversion efficiency is further tunable with rotation of one layer over other in the heterostructures. Our study demonstrates that PtSSe/ζ-Phosphorene heterostructure is potential candidate for photocatalytic water splitting.

Data availability

All data generated or analysed during this study are included in this published article [and its supplementary information files].

References

1. Liu, J. et al. Metal-free efficient photocatalyst for stable visible water splitting via a two-electron pathway. *Science* **347**, 970–974 (2015).
2. Chen, S., Takata, T. & Domen, K. Particulate photocatalysts for overall water splitting. *Nat. Rev. Mater.* **2**, 1–17 (2017).
3. Liu, C. et al. Two-dimensional materials for next-generation computing technologies. *Nat. Nanotechnol.* **15**, 545–557 (2020).

4. Faraji, M. et al. Two-dimensional materials in semiconductor photoelectrocatalytic systems for water splitting. *Energy Environ. Sci.* **12**, 59–95 (2019).
5. Li, X. T., Yang, C. L., Zhao, W. K. & Liu, Y. L. Photocatalytic Z-scheme overall water splitting for hydrogen generation with Sc2CCl2/ML (ML = MoTe2, Hf2CO2) heterostructures. *Int. J. Hydrog. Energy* **59**, 214–223 (2024).
6. Kim, K. et al. Van Der Waals heterostructures with high accuracy rotational alignment. *Nano Lett.* **16**, 1989–1995 (2016).
7. Xia, W. et al. Recent progress in Van Der Waals heterojunctions. *Nanoscale* **9**, 4324–4365 (2017).
8. Chen, X. et al. Recent progress on Van Der Waals heterojunctions applied in photocatalysis. *J. Mater. Chem. A* **10**, 7604–7625 (2022).
9. Sun, R., Yang, C. L., Wang, M. S. & Ma, X. G. High solar-to-hydrogen efficiency photocatalytic hydrogen evolution reaction with the HfSe2/InSe heterostructure. *J. Power Sources* **547**, 232008 (2022).
10. Meng, J., Wang, J., Wang, J., Li, Q. & Yang, J. C7N6/Sc2CCl2 weak Van Der Waals heterostructure: A promising visible-light-driven Z-scheme water splitting photocatalyst with interface ultrafast carrier recombination. *J. Phys. Chem. Lett.* **13**, 1473–1479 (2022).
11. Yin, Q. K., Yang, C. L., Wang, M. S. & Ma, X. G. Two-dimensional AuSe/SnSe heterostructure for solar photocatalytic hydrogen evolution reaction with Z-scheme. *Sol. Energy Mater. Sol. Cells* **247**, 111940 (2022).
12. Shi, A. et al. Direct Z-scheme photocatalytic system: Insights into the formative factors of photogenerated carriers transfer channel from ultrafast dynamics. *ACS Catal.* **12**, 9570–9578 (2022).
13. Geim, A. K. & Grigorieva, I. V. Van Der Waals heterostructures. *Nature* **499**, 419–425 (2013).
14. Novoselov, K. S., Mishchenko, A., Carvalho, A. & Castro Neto, A. 2D materials and Van Der Waals heterostructures. *Science* **353**, aac9439 (2016).
15. Wan, X. Q., Yang, C. L., Li, X. H., Wang, M. S. & Ma, X. G. Insights into photogenerated carrier dynamics and overall water splitting of the CrS3/GeSe heterostructure. *J. Phys. Chem. Lett.* **14**, 9126–9135 (2023).
16. Hong, X. et al. Ultrafast charge transfer in atomically thin MoS2/WS2 heterostructures. *Nat. Nanotechnol.* **9**, 682–686 (2014).
17. Zheng, Q. et al. Phonon-assisted ultrafast charge transfer at Van Der Waals heterostructure interface. *Nano Lett.* **17**, 6435–6442 (2017).
18. Long, R. & Prezhdo, O. V. Quantum coherence facilitates efficient charge separation at a MoS2/MoSe2 Van Der Waals junction. *Nano Lett.* **16**, 1996–2003 (2016).
19. Ceballos, F., Bellus, M. Z., Chiu, H. Y. & Zhao, H. Ultrafast charge separation and indirect exciton formation in a MoS2–MoSe2 Van Der Waals heterostructure. *ACS Nano* **8**, 12717–12724 (2014).
20. Zhou, Z., Niu, X., Zhang, Y. & Wang, J. Janus MoSSe/WSeTe heterostructures: A direct Z-scheme photocatalyst for hydrogen evolution. *J. Mater. Chem. A* **7**, 21835–21842 (2019).
21. Ma, H. et al. Enhancing the photoinduced interlayer charge transfer and spatial separation in Type-II heterostructure of WS2 and asymmetric Janus-MoSSe with intrinsic self-build electric field. *J. Phys. Chem. Lett.* **13**, 8484–8494 (2022).
22. Sant, R. et al. Synthesis of epitaxial monolayer Janus SPtSe. *npj 2D Mater. Appl.* **4**, 41 (2020).
23. Brent, J. R. et al. Production of few-layer phosphorene by liquid exfoliation of black phosphorus. *Chem. Commun.* **50**, 13338–13341 (2014).
24. Zeng, J., Cui, P. & Zhang, Z. Half layer by half layer growth of a blue phosphorene monolayer on a GaN (001) substrate. *Phys. Rev. Lett.* **118**, 046101 (2017).
25. Zhang, S. et al. Semiconducting group 15 monolayers: A broad range of band gaps and high carrier mobilities. *Angew. Chem.* **128**, 1698–1701 (2016).
26. Peng, R., Ma, Y., Huang, B. & Dai, Y. Two-dimensional Janus PtSSe for photocatalytic water splitting under the visible or infrared light. *J. Mater. Chem. A* **7**, 603–610 (2019).
27. Wang, G., Pandey, R. & Karna, S. P. Phosphorene oxide: Stability and electronic properties of a novel two-dimensional material. *Nanoscale* **7**, 524–531 (2015).
28. Pei, Q. X., Zhang, X., Ding, Z., Zhang, Y. Y. & Zhang, Y. W. Thermal stability and thermal conductivity of phosphorene in phosphorene/graphene Van Der Waals heterostructures. *Phys. Chem. Chem. Phys.* **19**, 17180–17186 (2017).
29. Boukhvalov, D., Rudenko, A., Prishchenko, D., Mazurenko, V. & Katsnelson, M. Chemical modifications and stability of phosphorene with impurities: A first principles study. *Phys. Chem. Chem. Phys.* **17**, 15209–15217 (2015).
30. Gao, J., Zhang, G. & Zhang, Y. W. Vastly enhancing the chemical stability of phosphorene by employing an electric field. *Nanoscale* **9**, 4219–4226 (2017).
31. Zhang, J. et al. Thermal conductivities of phosphorene allotropes from first-principles calculations: A comparative study. *Sci. Rep.* **7**, 4623 (2017).
32. Prezhdo, O. V. Mean field approximation for the stochastic Schrödinger equation. *J. Chem. Phys.* **111**, 8366–8377 (1999).
33. Gerber, I. C. & Marie, X. Dependence of band structure and exciton properties of encapsulated WSe 2 monolayers on the hBN-layer thickness. *Phys. Rev. B* **98**, 245126 (2018).
34. Zollner, K., Faria Junior, P. E. & Fabian, J. Strong manipulation of the valley splitting upon twisting and gating in MoSe 2/CrI 3 and WSe 2/CrI 3 Van Der Waals heterostructures. *Phys. Rev. B* **107**, 035112 (2023).
35. Volmer, F. et al. Twist angle dependent interlayer transfer of valley polarization from excitons to free charge carriers in WSe2/MoSe2 heterobilayers. *npj 2D Mater. Appl.* **7**, 58 (2023).
36. Kresse, G. & Furthmüller, J. Efficient iterative schemes for ab initio total-energy calculations using a plane-wave basis set. *Phys. Rev. B* **54**, 11169 (1996).
37. Kresse, G. & Joubert, D. From ultrasoft pseudopotentials to the projector augmented-wave method. *Phys. Rev. B* **59**, 1758 (1999).
38. Perdew, J. P., Burke, K. & Ernzerhof, M. Generalized gradient approximation made simple. *Phys. Rev. Lett.* **77**, 3865 (1996).
39. Monkhorst, H. J. & Pack, J. D. Special points for Brillouin-Zone integrations. *Phys. Rev. B* **13**, 5188 (1976).
40. Grimme, S., Antony, J., Ehrlich, S. & Krieg, H. A consistent and accurate ab initio parametrization of density functional dispersion correction (DFT-D) for the 94 elements H-Pu. *J. Chem. Phys.* **132** (2010).
41. Nosé, S. A unified formulation of the constant temperature molecular dynamics methods. *J. Chem. Phys.* **81**, 511–519 (1984).
42. Hoover, W. G. Canonical dynamics: Equilibrium phase-space distributions. *Phys. Rev. A* **31**, 1695 (1985).
43. Zheng, Q. et al. Ab initio nonadiabatic molecular dynamics investigations on the excited carriers in condensed matter systems. *Wiley Interdiscip. Rev. Comput. Mol. Sci.* **9**, e1411 (2019).
44. Lazić, P. & CellMatch Combining two unit cells into a common supercell with minimal strain. *Comput. Phys. Commun.* **197**, 324–334 (2015).
45. Ge, X., Zhou, X., Sun, D. & Chen, X. First-principles study of structural and electronic properties of monolayer PtX2 and Janus PtXY (X, Y = S, Se, and Te) via strain engineering. *ACS Omega* **8**, 5715–5721 (2023).
46. Sino, P. A. L. et al. Anisotropic rashba splitting in Pt-based Janus monolayers PtXY (X, Y = S, Se, or Te). *Nanoscale Adv.* **3**, 6608–6616 (2021).
47. Jyothi, M., Nagarajan, V. & Chandiramouli, R. Adsorption studies of 2, 3-butanedione and acetic acid on ζ-phosphorene sheets based on the first-principles study. *Comput. Theor. Chem.* **1208**, 113548 (2022).
48. Tao, W. L. et al. Thermoelectric properties of Janus MXY (M = pd, pt; X, Y = S, Se, Te) transition-metal dichalcogenide monolayers from first principles. *J. Appl. Phys.* **127**, 035101 (2020).
49. Liu, Z. et al. Interlayer binding energy of graphite: A mesoscopic determination from deformation. *Phys. Rev. B* **85**, 205418 (2012).
50. Björkman, T., Gulans, A., Krasheninnikov, A. V. & Nieminen, R. M. van der Waals bonding in layered compounds from advanced density-functional first-principles calculations. *Phys. Rev. Lett.* **108**, 235502 (2012).

51. Mouhat, F. & Coudert, F. X. Necessary and sufficient elastic stability conditions in various crystal systems. *Phys. Rev. B* **90**, 224104 (2014).
52. Frantsevich, I. N. Elastic constants and elastic moduli of metals and insulators. *Reference book* (1982).
53. Fu, C. F., Luo, Q., Li, X. & Yang, J. Two-dimensional Van Der Waals nanocomposites as Z-scheme type photocatalysts for hydrogen production from overall water splitting. *J. Mater. Chem. A* **4**, 18892–18898 (2016).
54. Wang, Y. & Long, R. Rapid decoherence induced by light expansion suppresses charge recombination in mixed cation perovskites: Time-domain ab initio analysis. *J. Phys. Chem. Lett.* **11**, 1601–1608 (2020).
55. He, J., Fang, W. H., Long, R. & Prezhdo, O. V. Superoxide/peroxide chemistry extends charge carriers' lifetime but undermines chemical stability of CH3NH3PbI3 exposed to oxygen: Time-domain ab initio analysis. *J. Am. Chem. Soc.* **141**, 5798–5807 (2019).
56. Wang, S., Luo, Q., Fang, W. H. & Long, R. Interfacial engineering determines band alignment and steers charge separation and recombination at an inorganic perovskite quantum dot/WS2 junction: A time domain ab initio study. *J. Phys. Chem. Lett.* **10**, 1234–1241 (2019).
57. Wang, W. et al. Femtosecond time-resolved spectroscopic observation of long-lived charge separation in bimetallic sulfide/g-C3N4 for boosting photocatalytic H2 evolution. *Appl. Catal. B* **282**, 119568 (2021).
58. Gao, Y., Fu, C., Hu, W. & Yang, J. Designing direct Z-scheme heterojunctions enabled by edge-modified phosphorene nanoribbons for photocatalytic overall water splitting. *J. Phys. Chem. Lett.* **13**, 1–11 (2021).
59. Niu, X., Bai, X., Zhou, Z. & Wang, J. Rational design and characterization of direct Z-scheme photocatalyst for overall water splitting from excited state dynamics simulations. *ACS Catal.* **10**, 1976–1983 (2020).
60. Bardeen, J. & Shockley, W. Deformation potentials and mobilities in non-polar crystals. *Phys. Rev.* **80**, 72 (1950).
61. Cai, Y., Zhang, G. & Zhang, Y. W. Polarity-reversed robust carrier mobility in monolayer MoS2 nanoribbons. *J. Am. Chem. Soc.* **136**, 6269–6275 (2014).
62. Kumar, A., Sachdeva, G., Pandey, R. & Karna, S. P. Optical absorbance in multilayer two-dimensional materials: Graphene and antimonene. *Appl. Phys. Lett.* **116**, 263102 (2020).
63. Matthes, L., Gori, P., Pulci, O. & Bechstedt, F. Universal infrared absorbance of two-dimensional honeycomb group-IV crystals. *Phys. Rev. B* **87**, 035438 (2013).
64. Chen, S. & Wang, L. W. Thermodynamic oxidation and reduction potentials of photocatalytic semiconductors in aqueous solution. *Chem. Mater.* **24**, 3659–3666 (2012).
65. Nørskov, J. K. et al. Origin of the overpotential for oxygen reduction at a fuel-cell cathode. *J. Phys. Chem. B* **108**, 17886–17892 (2004).
66. Jamdagni, P., Kumar, A., Srivastava, S., Pandey, R. & Tankeshwar, K. Photocatalytic properties of anisotropic β-PtX 2 (X = S, Se) and Janus β-PtSSe monolayers. *Phys. Chem. Chem. Phys.* **24**, 22289–22297 (2022).
67. Rouzhahong, Y., Wushuer, M., Mamat, M., Wang, Q. & Wang, Q. First principles calculation for photocatalytic activity of GaAs monolayer. *Sci. Rep.* **10**, 9597 (2020).
68. Li, H. et al. Adjustable photocatalytic ability of monolayer g-C3N4 utilizing single–metal atom: Density functional theory. *Appl. Surf. Sci.* **457**, 735–744 (2018).
69. Fu, C. F. et al. Intrinsic electric fields in two-dimensional materials boost the solar-to-hydrogen efficiency for photocatalytic water splitting. *Nano Lett.* **18**, 6312–6317 (2018).
70. Fan, Y., Wang, J. & Zhao, M. Spontaneous full photocatalytic water splitting on 2D MoSe 2/SnSe 2 and WSe 2/SnSe 2 vdW heterostructures. *Nanoscale* **11**, 14836–14843 (2019).

Acknowledgements

Author contributions

P.C. performed the calculations and written original draft. A.K. supervised the work and review and edit the manuscript.

Declarations

Competing interests

The authors declare no competing interests.

Additional information

Supplementary Information The online version contains supplementary material available at https://doi.org/10.1038/s41598-024-72757-6.

Correspondence and requests for materials should be addressed to A.K.

Reprints and permissions information is available at www.nature.com/reprints.

Publisher's note Springer Nature remains neutral with regard to jurisdictional claims in published maps and institutional affiliations.